NAS CR-134524
TRW ER-7697

VACUUM THERMAL-MECHANICAL FATIGUE TESTING OF TWO IRON BASE HIGH TEMPERATURE ALLOYS

TOPICAL REPORT NO. 3

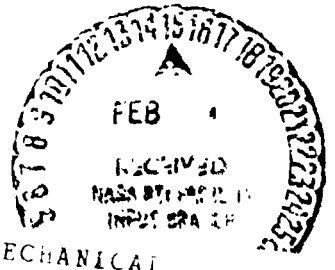

Prepared for

NATIONAL AERONAUTICS AND SPACE ADMINISTRATION

UNDER CONTRACT NAS-3-6010

TRW MATERIALS TECHNOLOGY LABORATORIES

CLEVELAND, OHIO

FOREWORD

The work described in this report was performed in the Materials Technology Laboratory of TRW Inc. under sponsorship of the National Aeronautics and Space Administration, Contract NAS-3-6010. The program was administered for TRW by Mr. J. A. Alexander, Program Manager. The Principal Investigator was Dr. K. D. Sheffler, with technical assistance provided by Mr. J. W. Sweeney. The NASA Technical Manager was Dr. G. R. Halford.

Prepared by: K. D. Sheffler cdk
K. D. Sheffler
Principal Engineer

Approved by: J. A. Alexander
J. A. Alexander
Manager
Materials Research Department

TABLE OF CONTENTS

I INTRODUCTION

Low cycle fatigue and thermal fatigue are recognized failure modes for structures such as gas turbine components which operate with combined temperature and strain cycling. The influence of temperature on low cycle fatigue life is well documented (1,2) but the mechanism by which temperature influences the fatigue process is not well understood. Low cycle fatigue life is generally acknowledged to be directly related to material ductility; however, ductility normally increases with temperature, whereas low cycle fatigue life normally decreases. Creep and environmental effects also influence low cycle fatigue behavior, but the relative contribution of these two factors is not well defined.

The subject of thermal fatigue, which involves combined temperature and strain cycling, is less well understood than isothermal elevated temperature fatigue. Most thermal fatigue studies have involved thermal cycling of specimens with complex geometries, where cyclic strain is generated by thermal expansion with geometric constraints. While useful for materials screening studies, this type of test suffers from the disadvantage that strain and temperature profiles are dictated by specimen geometry, and cannot be independently controlled.

A limited number of thermal fatigue studies have recently been conducted with independently controlled temperature and strain cycling (3-6). Results of these studies have indicated that fatigue life with thermal cycling is generally less than isothermal fatigue life at temperatures within the range of the thermal cycle. As with isothermal low cycle fatigue, no generalized mechanistic interpretation has evolved to explain thermal cycling effects. It is acknowledged that both creep and environmental effects are important. Creep is considered particularly important for unbalanced cycles where either tensile or compressive creep strain is reversed by nonthermally activated plastic flow. Manson has recently developed a strain range partitioning method for analysis of unreversed creep effects which has been used with good success to predict fatigue life with complex strain-temperature cycles (7).

The present study was undertaken to provide additional data for evaluation of the strain range partitioning concept, and to provide further insight into the mechanism for fatigue life variations with combined strain-temperature cycling. Results of recent vacuum thermal fatigue tests on two tantalum alloys have indicated that unreversed grain boundary sliding may be more damaging than unreversed homogeneous thermally activated flow (5). The present study was an extension of the tantalum study to two high temperature iron base alloys (A-286 and 304 stainless steel), with testing being conducted in vacuum to separate environmental effects from intrinsic effects of temperature on material behavior. The influence of thermal cycling on fatigue life was interpreted within the framework of the strain-range partitioning concept by correlating microstructural damage with various types of reversed inelastic strain cycles involving reversed and unreversed tensile and compressive creep deformation.

II EXPERIMENTAL DETAILS

To separate the effects of temperature and environment on fatigue behavior, all tests were conducted in an ion-pumped ultrahigh vacuum chamber at pressures below 1×10^{-7} torr. Elevated temperature isothermal fatigue tests were conducted on 304 stainless steel and A-286 alloy at two frequencies (0.65 and 0.0065 Hz) to evaluate the relative contribution of creep effects to the fatigue process. Test temperatures for the isothermal tests were 1200°F (922°K) for the 304 stainless steel and 1100°F (866°K) for the A-286 alloy. Tests with combined temperature and strain cycling were of two types, as illustrated in Figure 1. The thermal cycled in-phase square wave (TCIPS) cycleinvolved isothermal tensile strain imposed at a high temperature reversed by isothermal compressive strain imposed at a low temperature. The thermal cycled out-of-phase square wave (TCOPS) cycle was similar except that the temperature and strain phasing were reversed. The upper temperatures for these tests were the same as the isothermal test temperatures. The lower temperature was 600°F (589°K) for both alloys. Tests were conducted over a range of strain amplitudes (as measured by the width of the hysteresis loop at zero load) versus cycles to failure. Fatigue failure was defined in all cases as complete separation of the specimen into two pieces. Fractured specimens were sectioned longitudinally and examined metallographically to evaluate the character of the microstructural damage associated with each of the applied cycle types.

Test procedures were essentially identical to those reported for previous tests in this laboratory (5,8). Briefly, the test apparatus was designed to perform completely reversed push-pull fatigue tests on hour-glass specimens using independently programmable temperature and strain control. Temperature was programmed using a thyratron-controlled 50 KV AC transformer for direct resistance heating of the specimen, while diametral strain was controlled directly using an LVDT type extensometer coupled to a programmable closed loop electrohydraulic servosystem. For tests with combined temperature and strain cycling, the output of the servoamplifier was electronically compensated for thermal expansion so that net mechanical strain was controlled directly.

Supplementary vacuum tensile, creep, and strain partitioning tests were also conducted on this program to provide baseline characterization data. Details of these tests are presented in the Apendix.

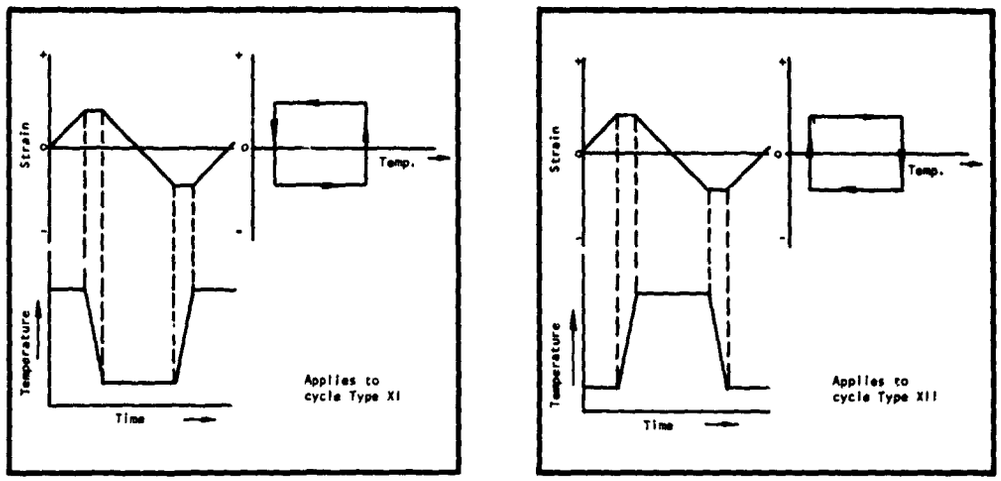

(a) TCIPS (b) TCOPS

Figure 1. Schematic representation of the two types of thermal-mechanical cycles applied in this study.

III RESULTS AND DISCUSSION

Test Results

Typical hysteresis loops generated with each of the four applied cycle types are shown in Figures 2 and 3. The isothermal loops were essentially symmetrical for both materials, with the load range developed at a constant diametral strain range being larger at the higher test frequency. The inelastic strain range developed in the A-286 alloy was smaller than that developed in the 304 stainless steel at an equivalent total diametral strain range because of the larger loads, and consequently larger elastic strains, developed in the higher strength material. Assymetric hysteresis loops were developed with both types of thermal fatigue cycles. This assymetry was caused by the difference in flow stress at the different temperature levels. In-phase cycling generated loops having a net compressive stress, while out-of-phase cycling caused a mean tensile stress to be developed.

In previous thermal cycled tests conducted in this laboratory (5) the occurrence of mean tensile and compressive stresses caused geometry changes to develop in the hourglass specimens during fatigue testing. These geometry changes involved thickening of the test specimen in locations above and below the minimum diameter with isothermal and in-phase cycling and thinning of the specimen in these same locations with out-of-phase cycling (Figure 4). Similar geometry changes were observed in the 304 stainless steel but not in the A-286 specimens tested in the current program (Figure 5). While no definite explanation is available for the occurrence of geometric instabilities in the 304 stainless steel but not in the A-286, it may be observed that the three alloys which have shown pronounced geometry changes in these types of tests (two tantalum alloys and 304 stainless steel) are basically high ductility materials, whereas the A-286 is a relatively low ductility alloy. It is not possible to determine from the available results if this qualitative correlation is representative of a general trend, or is merely coincidental. Additional data on a wider range of materials would be highly desirable to clarify this point.

The above noted geometry changes did not influence the fatigue life results for the isothermal and in-phase tests, since the change left the area of controlled maximum strain unchanged. However, the out-of-phase geometry change was thought to have a significant influence on fatigue life since this type of change caused failure to occur at a location separate from the original minimum diameter (Figure 5d). Thus, the failure site represented an area where strain was both unspecified and uncontrolled. This qualification applies only to the 304 stainless steel TCOPS results, since geometry changes were not observed in the A-286 alloy.

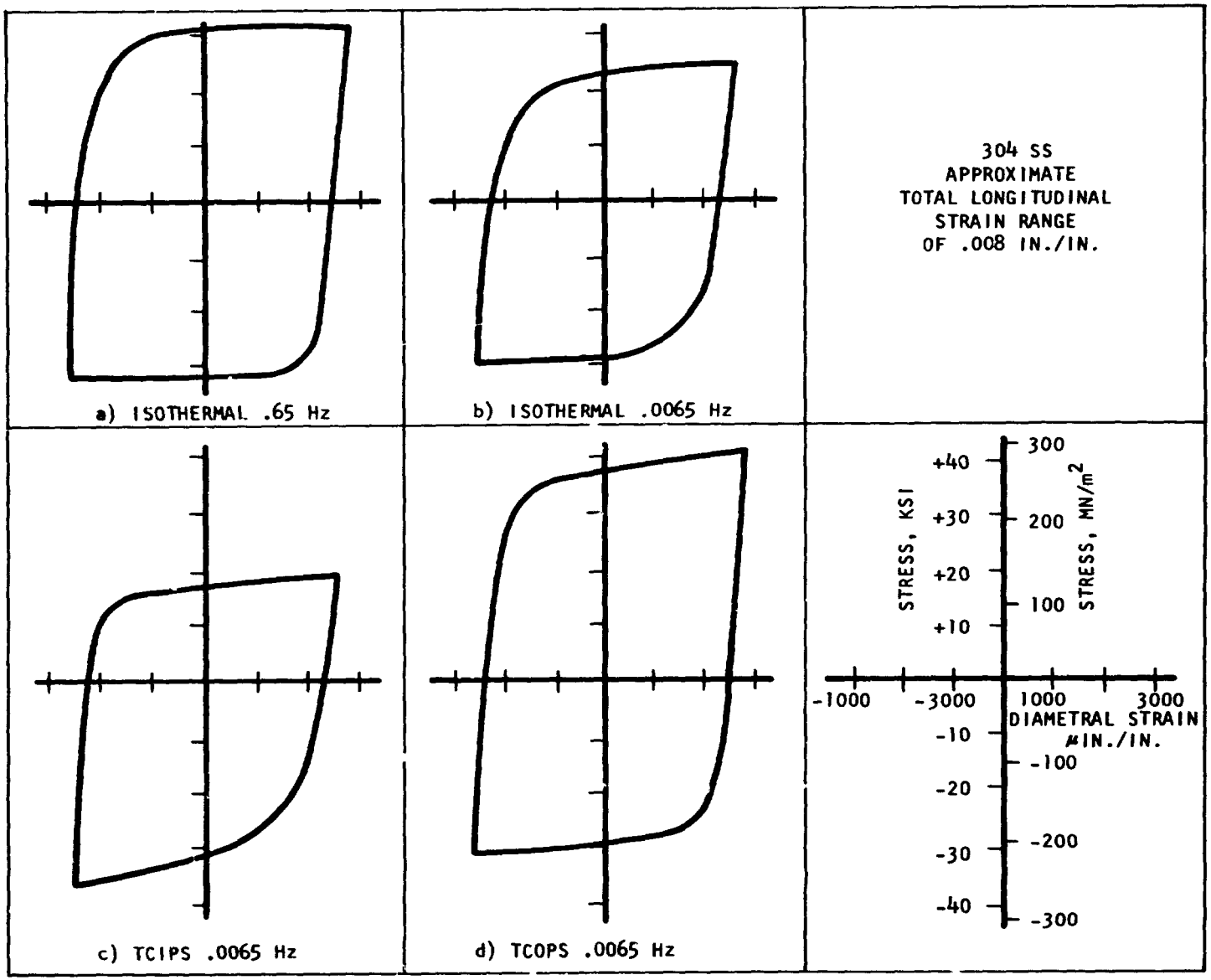

Figure 2. Typical hysteresis loops observed for 304 stainless steel tested with various strain-temperature cycles.

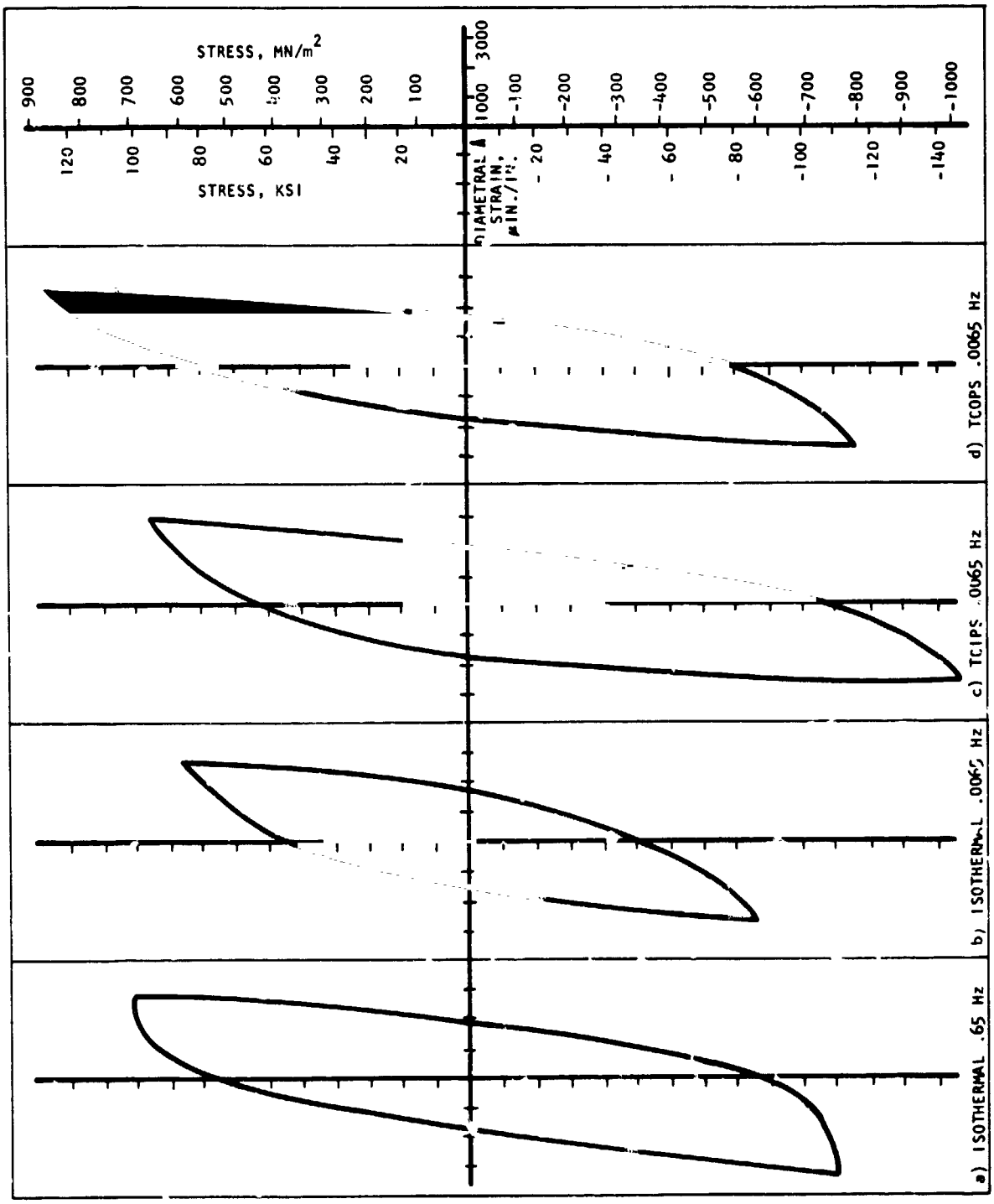

Figure 3. Typical hysteresis loops observed for A-286 alloy tested with various strain-temperature cycles.

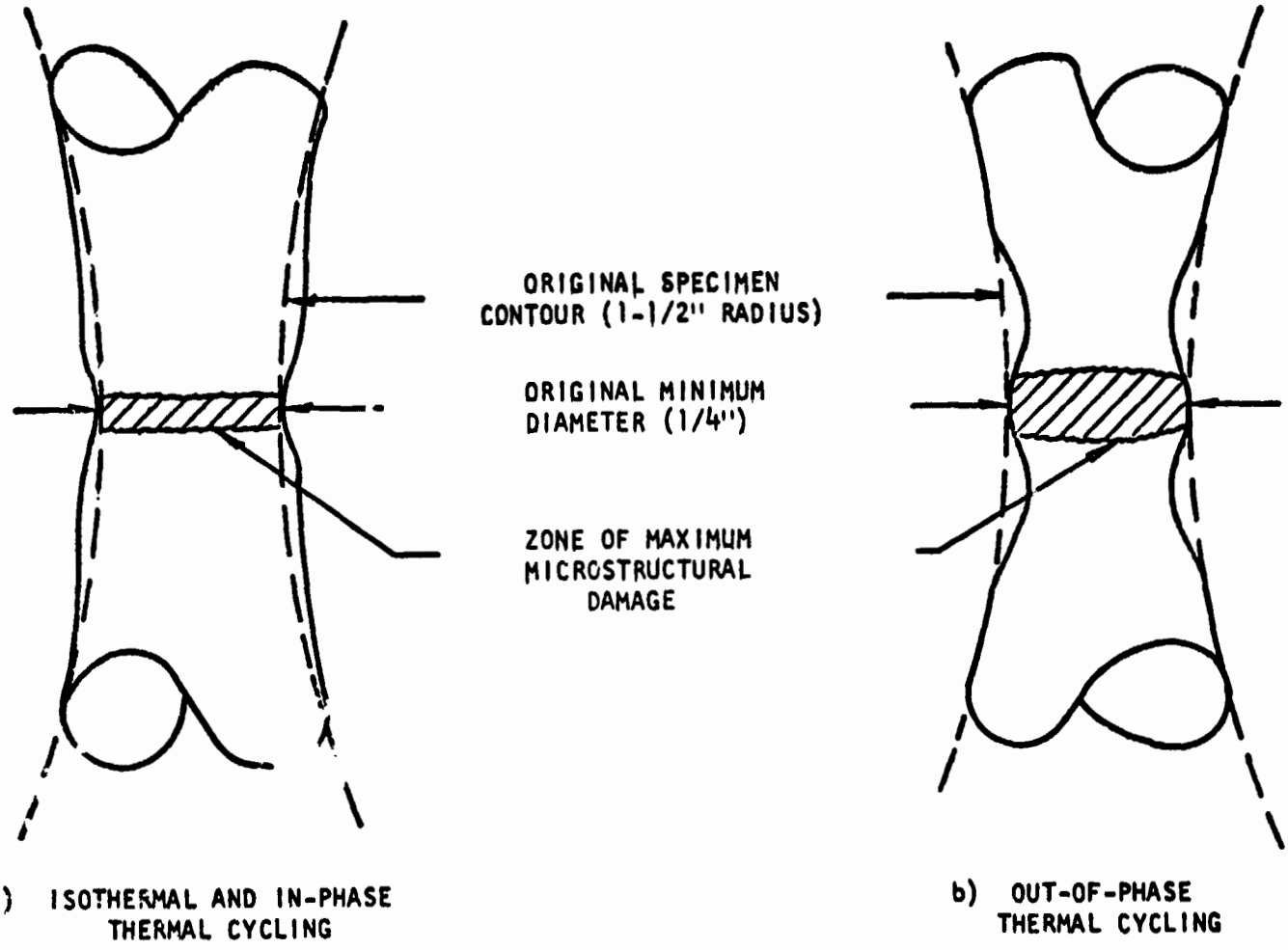

Figure 4. Schematic illustration of specimen geometry changes produced by thermal-mechanical fatigue cycling.

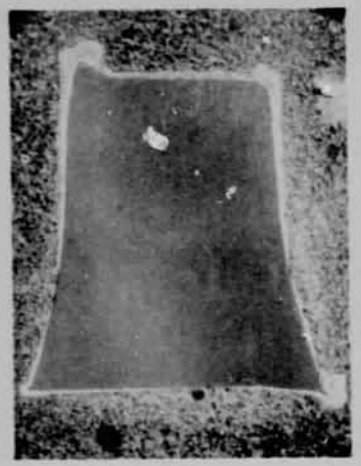

(a) 304 stainless steel, isothermal 1200°F (922°K), 0.65 Hz, longitudinal inelastic strain range 0.0108, cycles to failure 4483.

(b) 304 stainless steel, isothermal 1200°F (922°K), 0.0065 Hz, longitudinal inelastic strain range .0099, cycles to failure 3602.

(c) 304 stainless steel, TCIPS 1200/600°F (922/589°K), .0065 Hz, longitudinal inelastic strain range .0103, cycles to failure 455.

(d) 304 stainless steel, TCOPS 1200/600°F (922/589°K), .0065 Hz, longitudinal inelastic strain range .0100 cycles to failure 311.

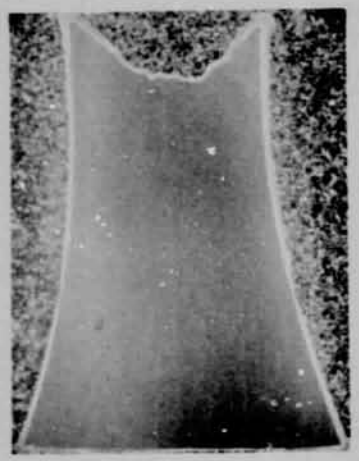

(e) A-286, isothermal 1100°F (866°K), 0.65 Hz, longitudinal inelastic strain range .0074, cycles to failure 3433.

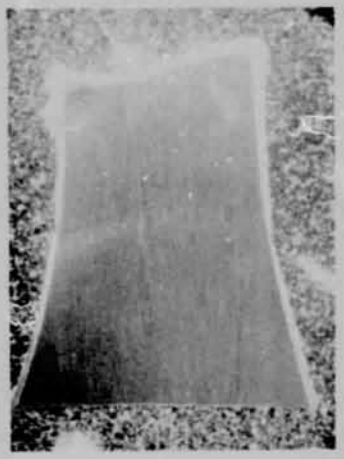

(f) A-286, isothermal 1100°F (866°K) .0065 Hz, longitudinal inelastic strain range .0072, cycles to failure 2319.

(g) A-286, TCIPS 1100/600°F (866/589°K), .0065 Hz, longitudinal inelastic strain range .0080, cycles to failure 350.

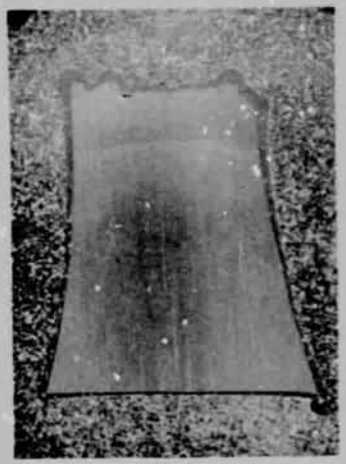

(h) A-286, TCOPS 1100/600°F (866/589°K), .0065 Hz, longitudinal inelastic strain range .0082, cycles to failure 938.

Figure 5. Illustrating geometry of fatigue tested hourglass specimens. Materials and test conditions as indicated. Note that apparent specimen lengths are not representative of actual length changes which occurred during testing. Original magnification 6X, reduced 40% for reproduction.

Fatigue life results for both alloys are summarized in Tables 1 and 2. The 304 stainless steel alloy displayed cyclic strain hardening, while the A-286 alloy exhibited cyclic strain softening. For both alloys, the majority of hardening or softening occurred during the first few cycles of testing. The stress ranges noted in Tables 1 and 2 represent stabilized loop sizes. For the thermal cycled tests, where assymetrical loops were observed, both tensile and compressive stress values are tabulated.

The life results from Tables 1 and 2 are plotted against longitudinal inelastic strain range in Figures 6 and 7. Also shown in these figures are life predictions made by the method of universal slopes using the tension test results noted in Appendix A. These experimental resuts indicate definite effects of both frequency and thermal cycling on fatigue life. Decreasing frequency, which increased the potential for creep effects, reduced fatigue life for both materials. Combined temperature and strain cycling caused further reductions of fatigue life as compared to isothermal cycling at the maximum temperature associated with the thermal cycle. For the A-286 alloy, the in-phase type of cycling was more damaging than out-of-phase cycling. For the 304 stainless steel alloy the reverse appeared to be true; however, the out-of-phase stainless steel results are confounded by the previously noted geometry change, so that is probable that the TCOPS 304 stainless steel data do not represent the intrinsic capability of the material to withstand out-of-phase thermal cycling. At the higher strain ranges, where the geometry change was most pronounced, the 304 TCOPS data were below the TCIPS results. However, at the lowest strain range, where the geometry change was smaller, the TCOPS life was larger than the TCIPS life. Based on previous results obtained on the tantalum alloys (5), it is considered probable that the TCOPS geometric instability would cease to occur, and that the position of the 304 stainless steel TCOPS fatigue curve might approach the isothermal fatigue curve for this material at lower strain ranges.

Microstructural Observations

Microstructural damage observed in the fatigue tested specimens varied with both cycle type and test material, as shown in Figures 8 through 15. Neither alloy showed evidence of significant internal damage with isothermal high frequency cycling (Figures 8a and 9a). Both alloys exhibited mixed mode cracking under these test conditions, as shown in Figures 8 and 9b and c. Some tendency for cracking at twin boundaries was also observed in the 304 stainless steel (Figure 8c). Some of the secondary cracks observed in A-286 appeared to be associated with carbide inclusions (Figure 9d). While this association was assumed to have some influence on cyclic life of the A-286 alloy, it was not thought to influence the life differences caused by different types of cycles, since the carbide associated cracking was observed in A-286 for all cycle types.

Table 1

304 Stainless Steel Fatigue Results

Test No.	Cycle Type*	Frequency Hz	Temperature Upper °F	Temperature Upper °K	Temperature Lower °F	Temperature Lower °K	Longitudinal Inelastic Strain Range (Dimensionless)	Stress ksi Tensile	Stress ksi Compressive	Stress ksi Range	Stress MN/m² Tensile	Stress MN/m² Compressive	Stress MN/m² Range	Cycle to Failure
A3A	Isothermal	0.65	1200	922	-	-	.0212	-	-	83.3	-	-	574	1219
A1A	Isothermal	0.65	1200	922	-	-	.0108	-	-	63.4	-	-	437	4483
A2A	Isothermal	0.65	1200	922	-	-	.0052	-	-	53.9	-	-	371	19016
A4A	Isothermal	0.0065	1200	922	-	-	.0216	-	-	70.3	-	-	484	557
A12A	Isothermal	0.0065	1200	922	-	-	.0099	-	-	55.3	-	-	331	3602
A7A	TCIPS	0.0065	1200	922	[illegible]	589	.0220	30.5	43.3	73.8	210	298	508	226
A8A	TCIPS	0.0065	1200	922	600	589	.0103	21.6	41.0	62.6	149	282	431	455
A5A	TCIPS	0.0065	1200	922	600	589	.0050	23.6	39.9	63.5	163	275	438	573
A11A	TCOPS	0.0065	1200	922	600	589	.0209	36.9	32.9	69.2	250	227	477	214
A6A	TCOPS	0.0065	1200	922	600	589	.0100	38.3	31.3	69.6	264	216	480	311
A9A	TCOPS	0.0065	1200	922	600	589	.0049	34.8	28.8	63.6	240	198	438	3612

* TCIPS - Thermal Cycled In-Phase Square Wave
TCOPS - Thermal Cycled Out-of-Phase Square Wave

Table 2

A-286 Alloy Fatigue Results

Test No.	Cycle Type*	Frequency Hz	Temperature Upper °F	Temperature Upper °K	Temperature Lower °F	Temperature Lower °K	Longitudinal Inelastic Strain Range (Dimensionless)	Stress ksi Tensile	Stress ksi Compressive	Stress ksi Range	Stress MN/m² Tensile	Stress MN/m² Compressive	Stress MN/m² Range	Cycle to Failure
L-42	Isothermal	0.65	1100	866	-	-	.0170	-	-	261	-	-	1798	432
L-41	Isothermal	0.65	1100	866	-	-	.0074	-	-	221	-	-	1523	3433
L-43	Isothermal	0.65	1100	866	-	-	.0033	-	-	200	-	-	1378	40,162
L-44	Isothermal	0.0065	1100	866	-	-	.0167	-	-	215	-	-	1481	358
L-45	Isothermal	0.0065	1100	866	-	-	.0072	-	-	193	-	-	1330	2319
L-50	TCIPS	0.0065	1100	866	600	589	.0183	115	153	268	792	1054	1846	104
L-46	TCIPS	0.0065	1100	866	600	589	.0080	95.6	148	244	660	1020	1680	350
L-47	TCIPS	0.0065	1100	866	600	589	.0026	86.3	121	207	594	834	1428	2371
L-51	TCOPS	0.0065	1100	866	600	589	.0180	153	113	266	1054	779	1833	[illegible]
L-52	TCOPS	0.0065	1100	866	600	589	.0082	118	111	229	813	765	1578	9

* TCIPS - Thermal Cycled In-Phase Square Wave
TCOPS - Thermal Cycled Out-of-Phase Square Wave

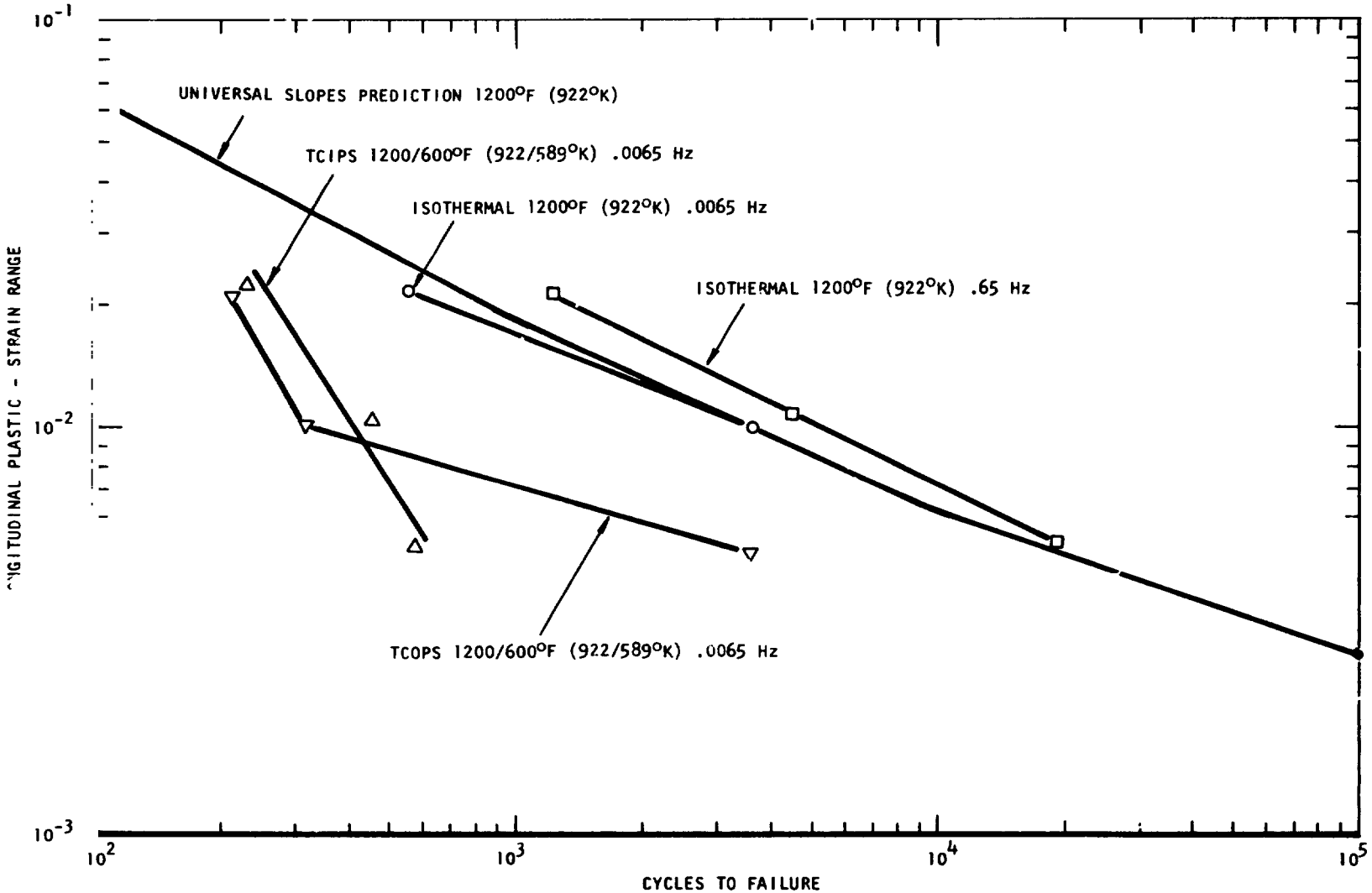

Figure 6. 304 stainless steel fatigue life results.

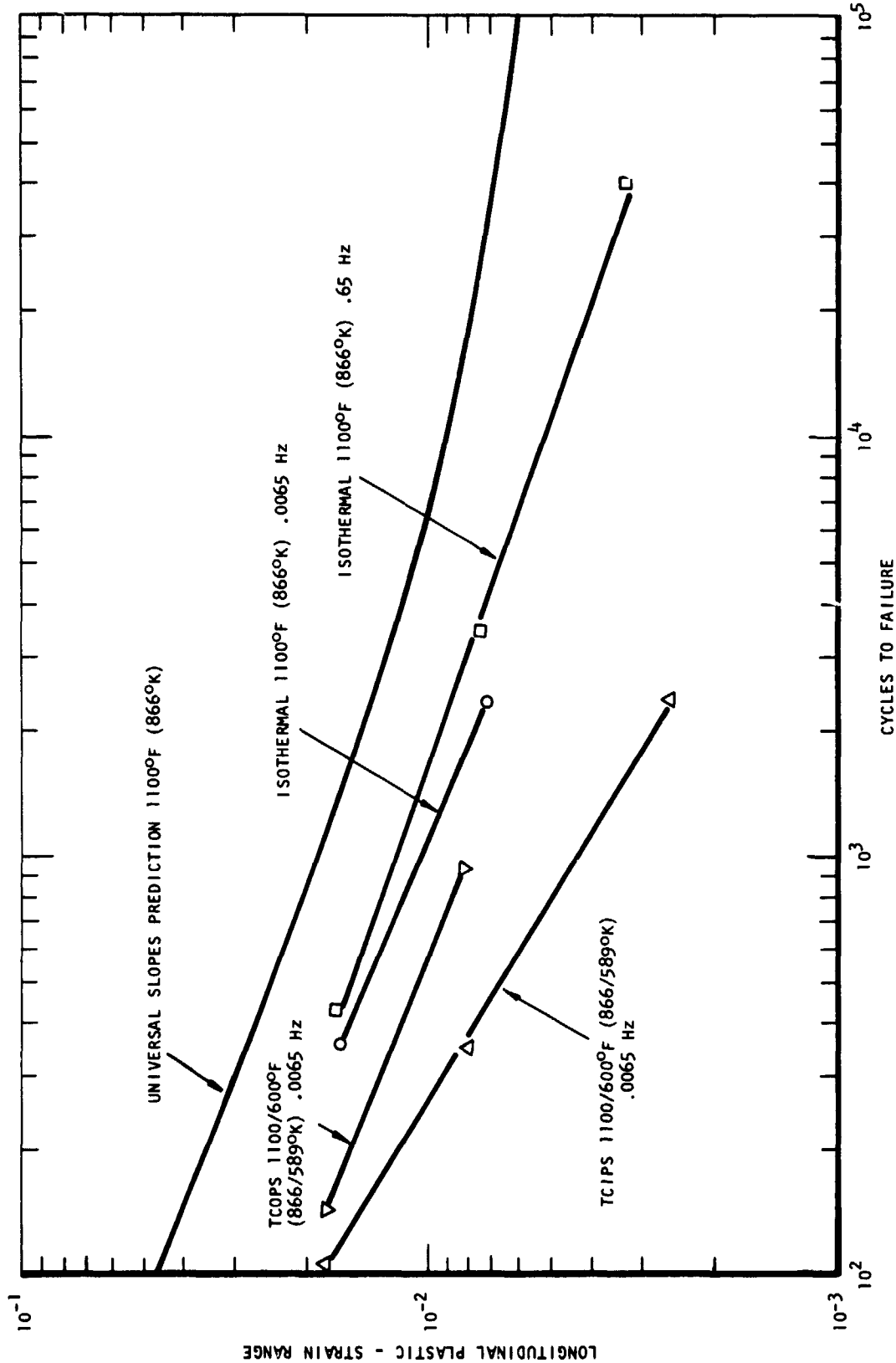

Figure 7. A-286 fatigue life results.

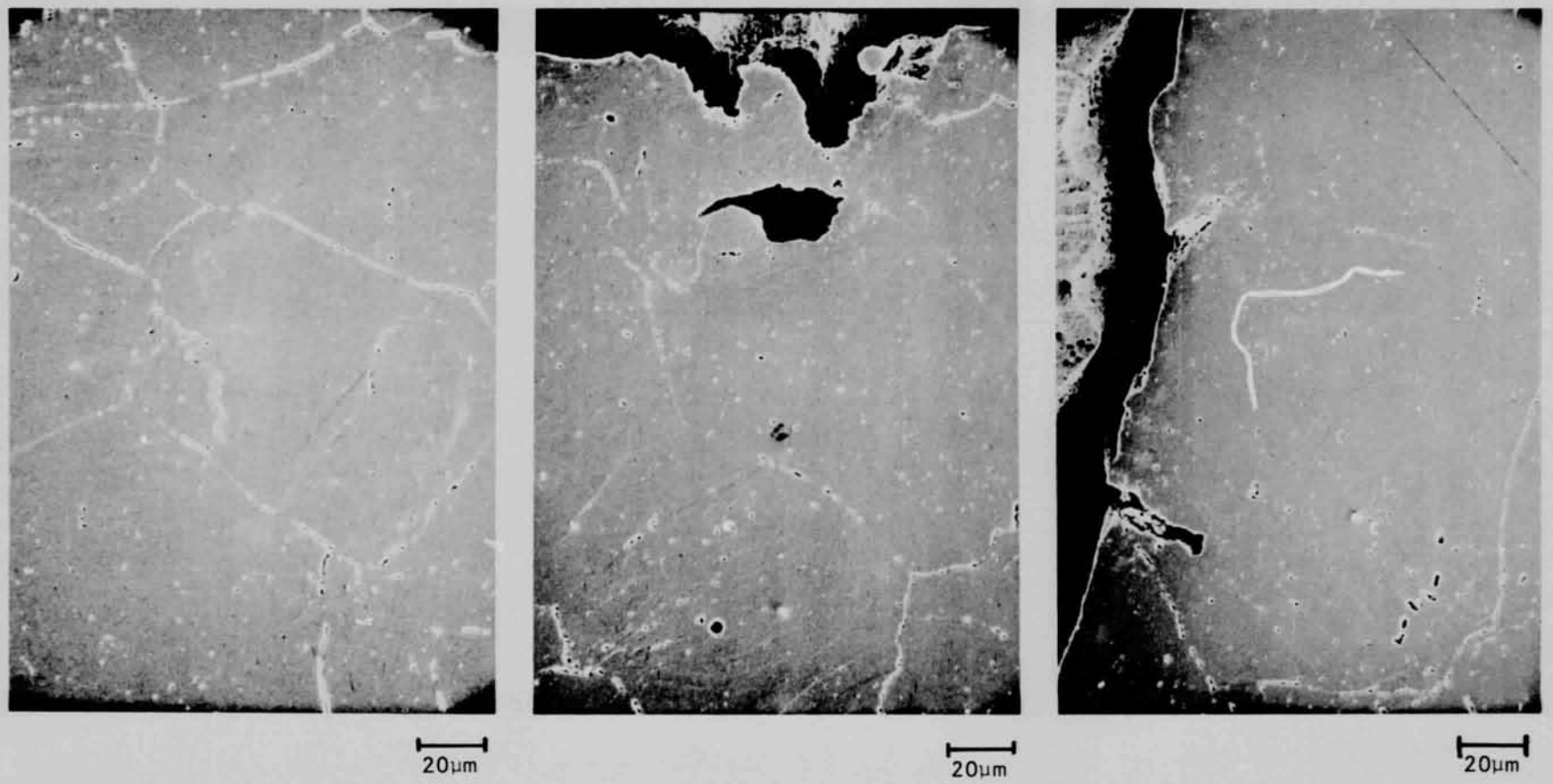

(a) Interior of specimen approximately .3mm below fracture surface

(b) Secondary grain boundary crack immediately below fracture surface.

(c) Transgranular and intergranular secondary cracks approximately 1.5mm below fracture surface.

Figure 8. 304 stainless steel fatigue tested isothermally at 1200°F (922°K), .65 Hz, longitudinal inelastic strain range 0.0108, cycles to failure 4483. Tensile axis parallel to long edge of photomicrographs. Magnification 500X

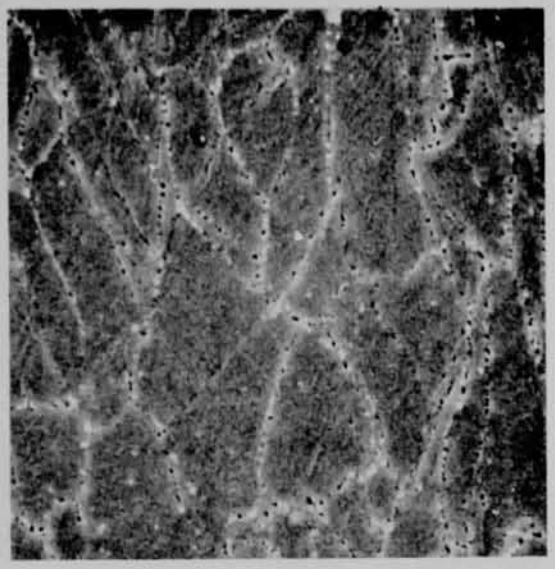

(a) Structure approximately 1.3mm below fracture surface.

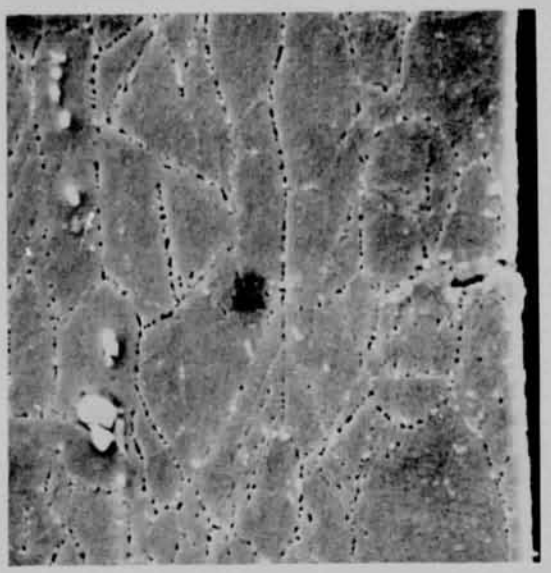

(b) Intergranular secondary crack approximately 1.6mm below fracture surface.

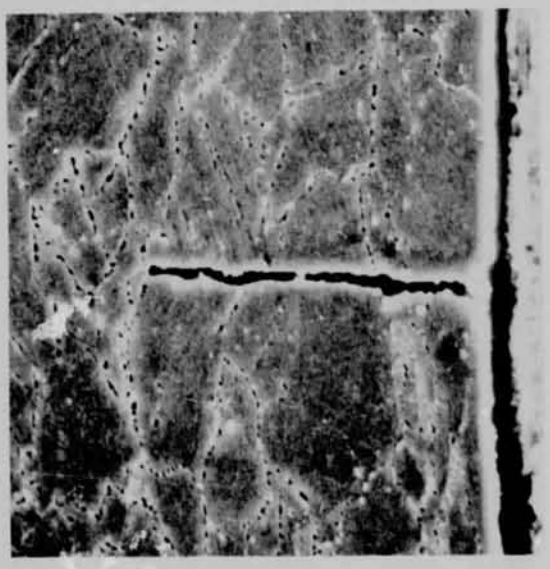

(c) Transgranular secondary crack approximately 2.25mm below fracture surface.

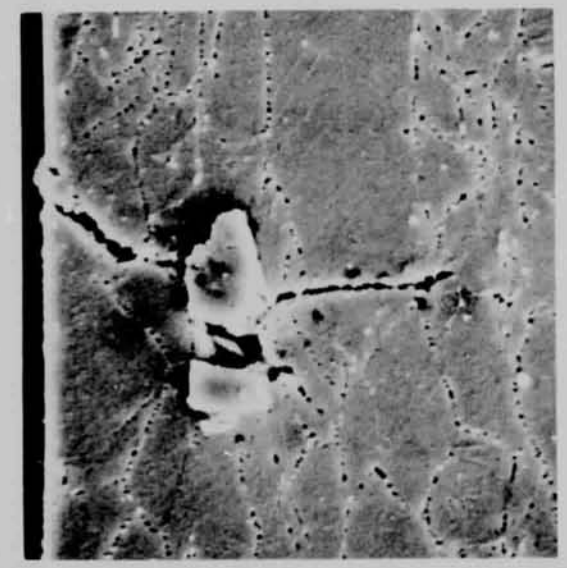

(d) Secondary crack associated with carbide approximately 2.6mm below fracture surface.

Figure 9. A-286 alloy fatigue tested isothermally at 1100°F (866°K), .65 Hz, longitudinal inelastic strain range 0.0074, cycles to failure 3433. Tensile axis vertical. Magnification 2000X.

Secondary cracking in the low frequency isothermal specimens was exclusively intergranular in both materials (Figures 10b and 11b). The A-286 alloy exhibited little internal damage except for the occasional appearance of carbide associated cracks (Figure 11). The 304 stainless steel alloy exhibited localized damage at grain and twin boundaries. This damage was characterized by boundary serration and localized intergranular cracking (Figure 10a).

In-phase thermal cycling caused severe internal grain boundary cavitation in both alloys (Figures 12 and 13). This grain boundary decohesion was assumed to be the cause of premature fatigue failure. Boundary cavitation was attributed to unreversed tensile grain boundary sliding generated by inelastic tensile strain introduced at a high temperature where grain boundary sliding occurs, and reversed by inelastic compressive strain at a low temperature where grain boundary sliding does not occur. Numerous carbide associated cracks were observed in the in-phase cycled A-286 alloy (Figure 13d).

Significant differences were observed between the types of damage found in the out-of-phase A-286 and 304 stainless steel specimens. Damage in the center of the "bulge" on the 304 stainless steel specimens consisted of extensive pitting which tended to be concentrated near grain boundaries (Figure 14a). This pitting was assumed to be an etching effect associated with areas of extremely high dislocation density. It is postulated that this structure was caused by intragranular strain adjacent to the grain boundaries which was required to accomodate accumulated compressive grain boundary sliding in the high temperature half cycle. The structure in the root of the secondary "neck" of the 304 stainless steel TCOPS specimen showed evidence of grain boundary cavitation (Figure 14b)*. Unfortunately, because of the instability problem, the temperature-strain history in the failure area was not known, and a specific failure mechanism could not be proposed.

In the lower ductility A-286 alloy, where unreversed compressive grain boundary dispiacements could not be fully accomodated by intragranular deformation, significant intergranular cavitation was observed (Figure 15a). Because the out-of-phase geometric instability did not occur in this alloy, it was possible to postulate cavitation as the direct cause of premature fatigue failure. A number of carbide associated cracks were also observed in the out-of-phase cycled A-286 alloy (Figure 15b). Secondary cracking was basically intergranular, as shown in Figure 15c.

- - - - - - - - - - - -

* This area also contained a number of unusual features having the appearance of "stringers," or nonmetallic inclusions parallel to the tensile axis. These features were not identified, but were not thought to be associated with the failure process.

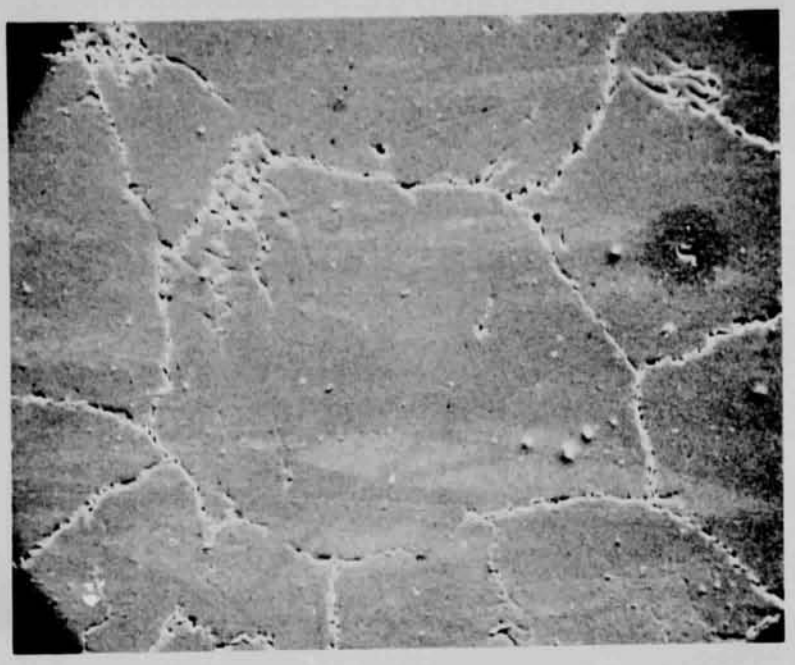

(a) Interior of specimen approximately .5mm below fracture surface.

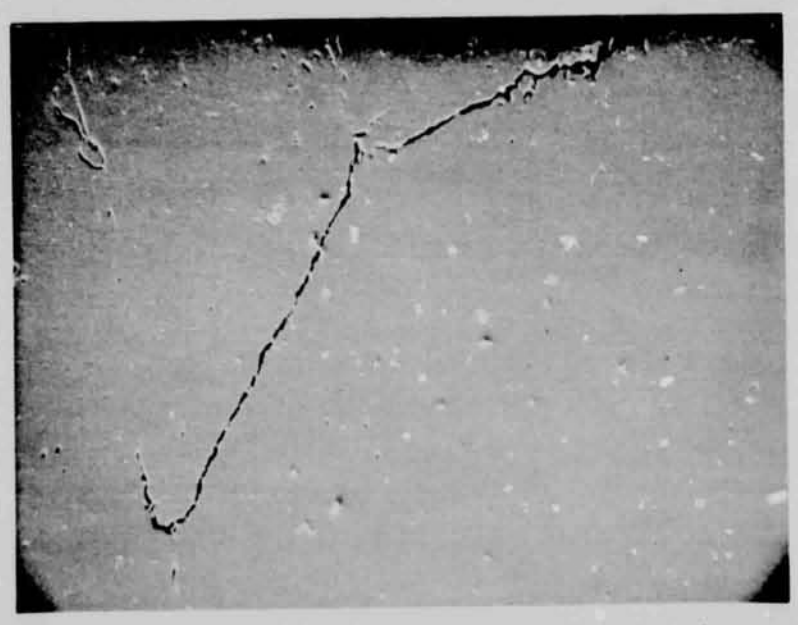

(b) Intergranular secondary crack approximately 1.8mm below fracture surface.

Figure 10. 304 stainless steel fatigue tested isothermally at 1200°F (922°K), .0065 Hz longitudinal inelastic strain range .0099, cycles tofailure 3602. Tensile axis parallel to long edge of photomicrographs. Magnification 1000X

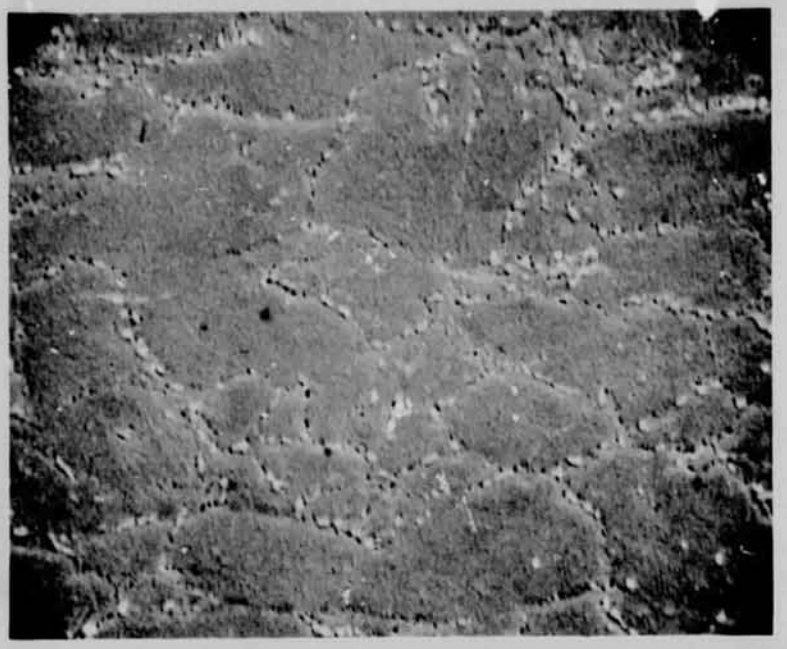

(a) Structure in interior of specimen approximately .3mm below fracture surface.

5μm

(b) Secondary crack approximately 1.8mm below fracture surface.

5μm

Figure 11. A-286 alloy fatigue tested isothermally at 1100°F (866°K), .0065 Hz, longitudinal inelastic strain range .0072, cycles to failure 2319. Tensile axis parallel to long dimension of photomicrograph. Magnification 2000X.

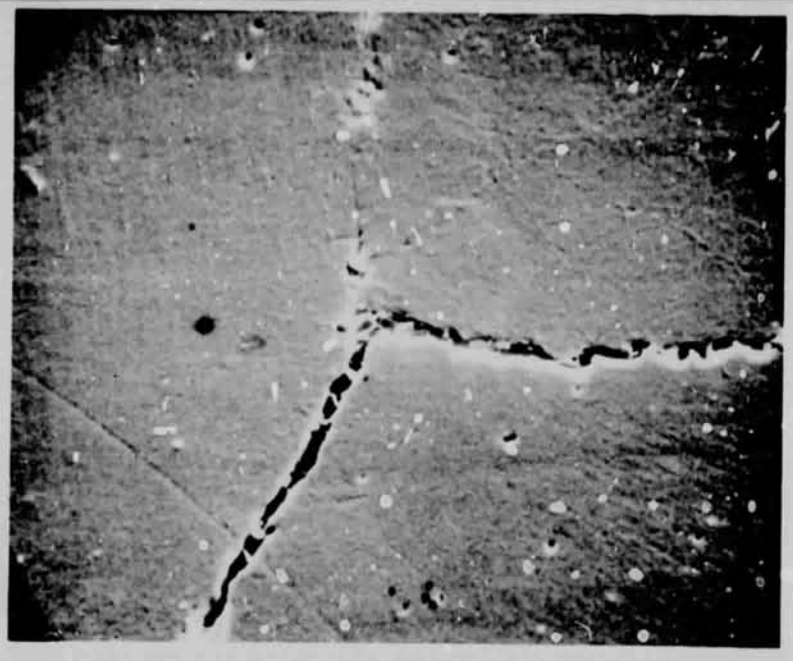

(a) Grain boundary decohesion in interior of specimen approximately 1.8mm below fracture surface. 2000X

5μm

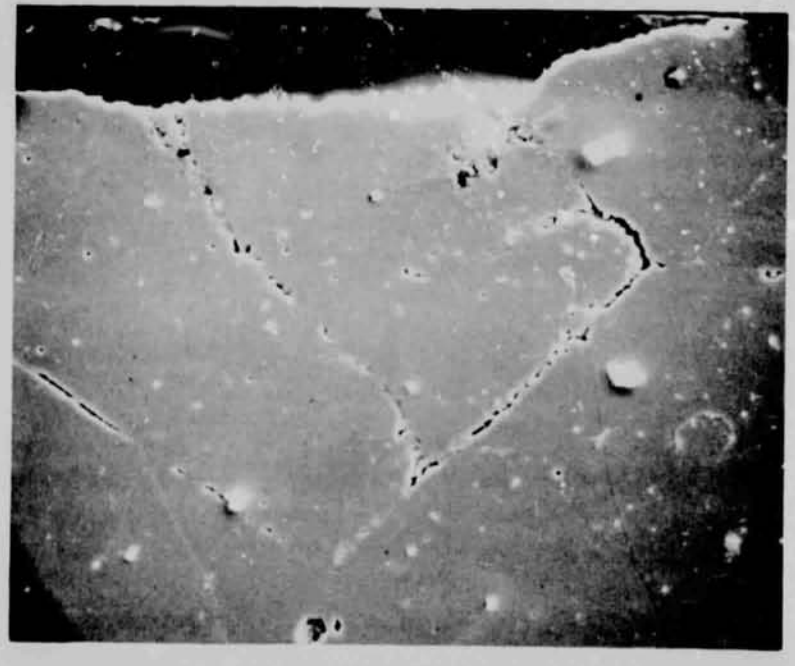

(b) Intergranular secondary cracking approximately 2.6mm below fracture surface. 1000X

10μm

Figure 12. 304 stainless steel fatigue tested with in-phase thermal cycling (tension isothermal at 1200°F (922°K); compression isothermal at 600°F (589°K), .0065 Hz, longitudinal inelastic strain range .0103, cycles to failure 455. Tensile axis parallel to long edge of photomicrograph.

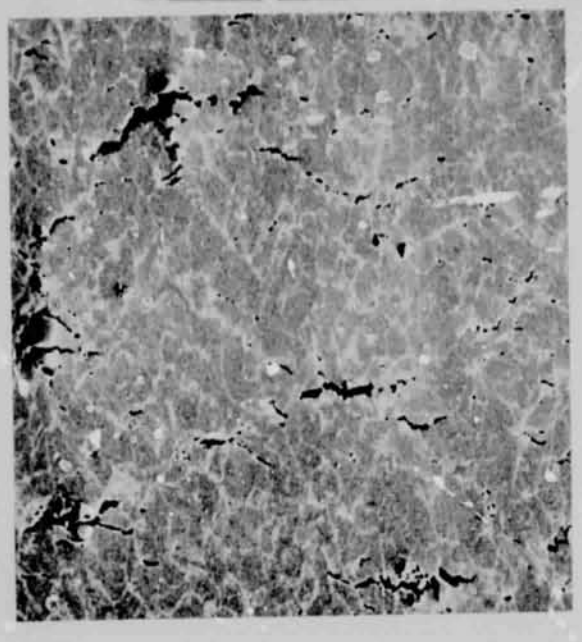

(a) Grain boundary decohesion approximately .3 mm below fracture surface. 500X

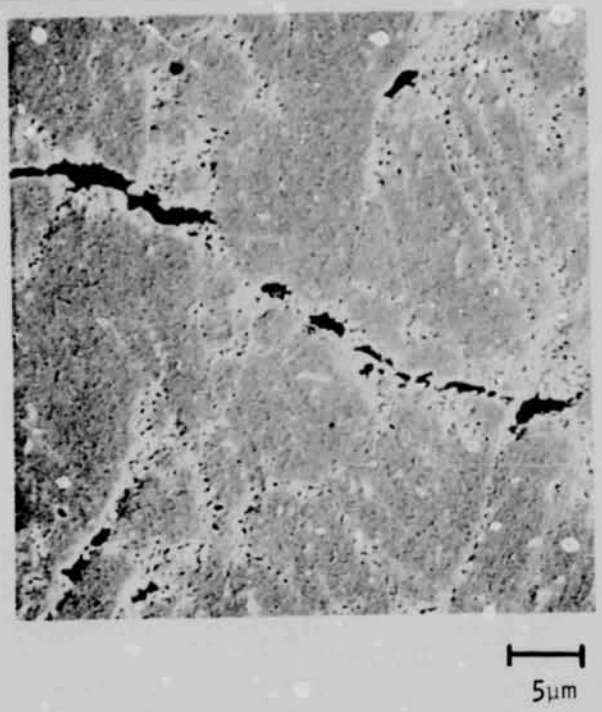

(b) Grain boundary decohesion approximately .3mm below fracture surface. 2000X

(c) Intergranular secondary crack approximately 1mm below fracture surface. 5000X

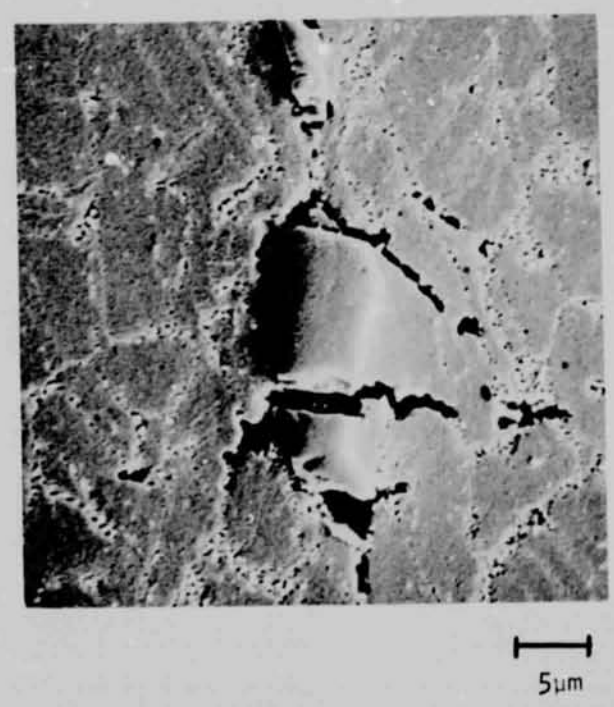

(d) Carbide initiated internal crack located approximately .3mm below fracture surface. 2000X

Figure 13. A-286 alloy fatigue tested with in-phase thermal cycling (tension isothermal at 1100°F (866°K), compression isothermal at 600°F (589°K), .0065 Hz, longitudinal inelastic strain range .0080, cycles to failure 350. Tensile axis vertical.

(a) Structure in center of "bulge". 500X

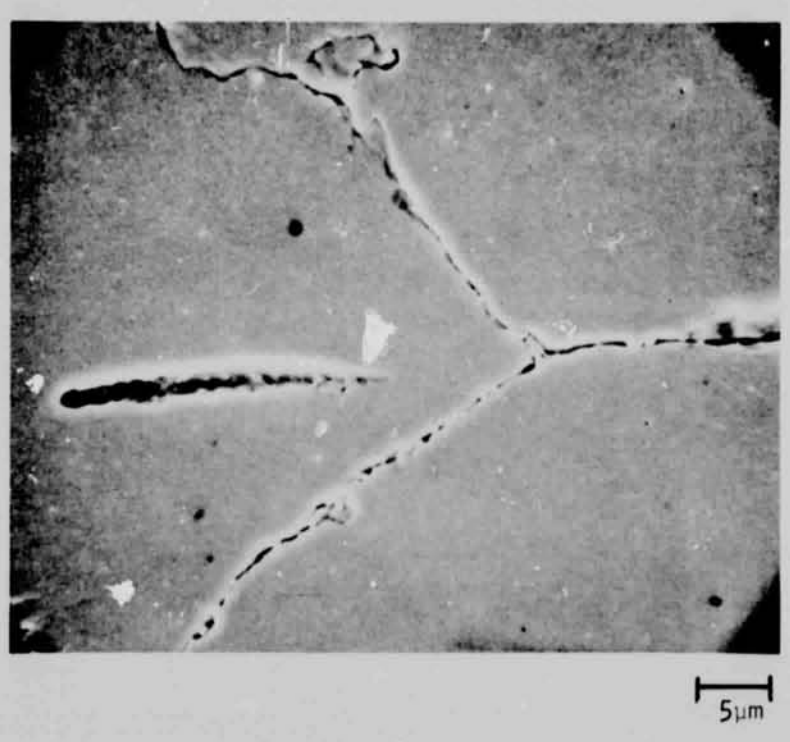

(b) Grain boundary decohesion in "necked" area. 2000X

Figure 14. 304 stainless steel fatigue tested with out-of-phase thermal cycling (tension isothermal at 600°F (589°K), compression isothermal at 1200°F (922°K), .0065 Hz, longitudinal inelastic strain range .0100, cycles to failure 311. Tensile axis parallel to long edge of photomicrograph.

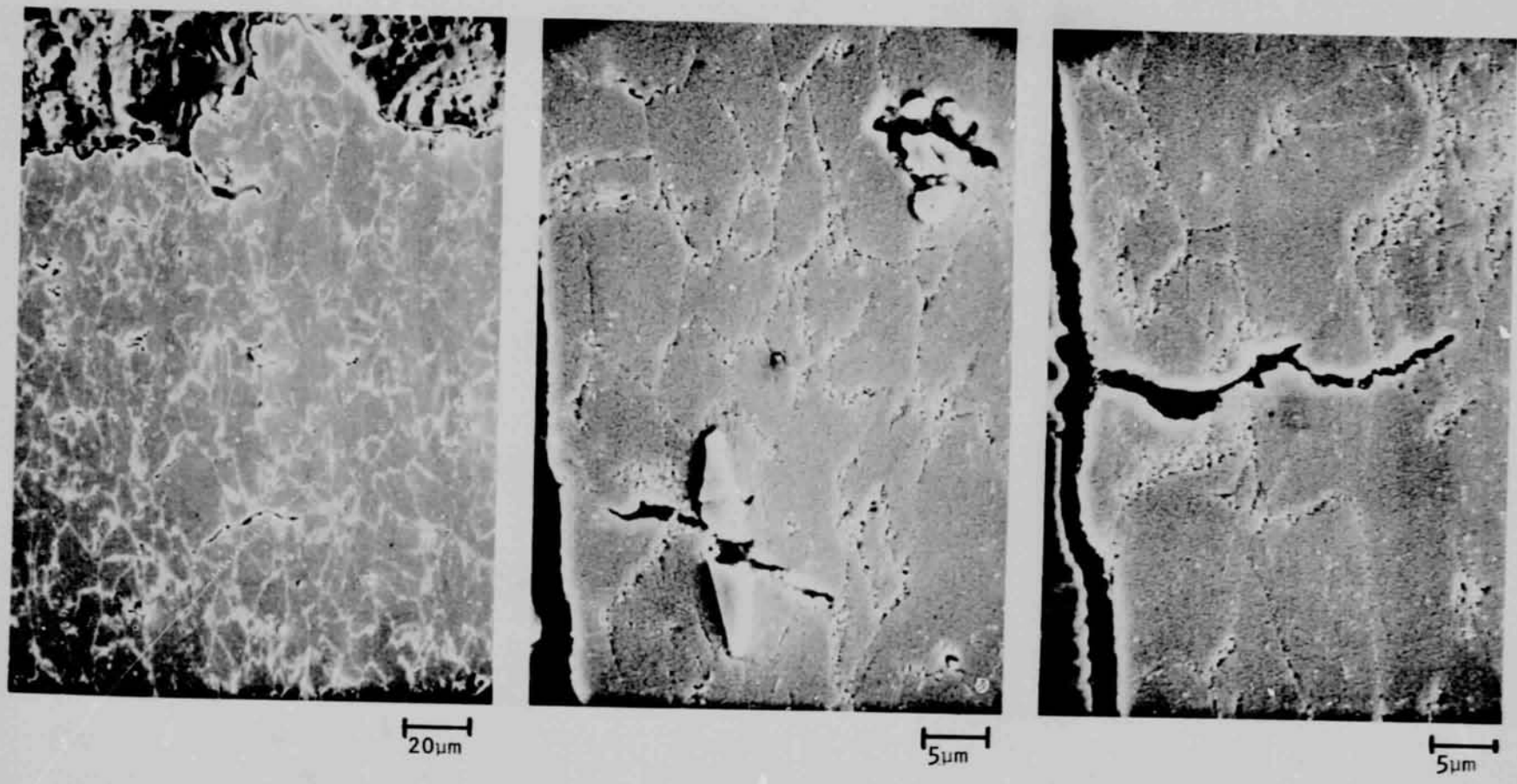

(a) Subsurface cracking in vicinity of fracture surface. 500X

(b) Carbide initiated internal cracking. 2000X

(c) Secondary crack approximately 0.5mm below fracture surface. 2000X

Figure 15. A-286 alloy tested without out-of-phase thermal cycling (tension isothermal at 600°F (589°K), compression isothermal at 1100°F (866°K), .0065 Hz, longitudinal inelastic strain range .0082, cycles to failure 938. Tensile axis parallel to long dimension of photomicrographs.

IV SUMMARY

Elevated temperature ultrahigh vacuum low cycle fatigue and thermal fatigue tests on 304 stainless steel and A-286 alloy have shown significant effects of frequency and of combined temperature-strain cycling on cyclic life. At temperatures in the creep range, fatigue lives of both materials were lower at .0065 Hz than at .65 Hz. Metallographic examination of fractured specimens indicated mixed mode (intergranular and transgranular) fracture at the higher frequency and exclusively intergranular fracture at the lower frequency. In-phase thermal cycling (tension at high temperature and compression at low temperature) caused large life reductions in both materials. These life reductions were attributed to grain boundary cavitation caused by unreversed grain boundary sliding. Out-of-phase thermal cycling (tension at low temperature and compression at high temperature) also caused large cyclic life reductions in both materials. These reductions were attributed to geometric instabilities in the 304 stainless steel and to grain boundary cavitation in the A-286 alloy. The proposed mechanism for development of out-of-phase cavitation damage in the A-286 alloy involved accumulation of unreversed compressive grain boundary displacements in a low ductility material where the displacements could not be fully accomodated by intragranular deformation.

V REFERENCES

1. A. E. Carden, A. J. McEvily, and C. H. Wells, ed., Fatigue at Elevated Temperatures, ASTM STP 520, August 1973.

2. S. S. Manson, Thermal Stress and Low Cycle Fatigue, McGraw Hill, New York, 1966.

3. A. E. Carden and T. B. Slede, "High Temperature Low Cycle Fatigue Experiments on Hastalloy X," p. 111 in ASTM STP 459, Fatigue at High Temperature, November 1969.

4. V. S. Lindholm and D. L. Davidson, "Low Cycle Fatigue with Combined Thermal and Strain Cycling," p. 473 in Ref. 1.

5. K. D. Sheffler and G. S. Doble, "Thermal Fatigue Behavior of T-111 and ASTAR 811C in Ultrahigh Vacuum," p. 491 in Ref. 1.

6. C. A. Rau, Jr., A. E. Gemma, and G. R. Leverant, "Thermal-Mechanical Fatigue Crack Propogation in Nickel- and Cobalt-Base Superalloys Under Various Strain-Temperature Cycles," p. 166 in Ref. 1.

7. S. S. Manson, G. R. Halford, and M. M. Hirschberg, "Design for Elevated Temperature Environment", American Society of Mechanical Engineers, 1971, pp. 12-24, discussion pp. 25-28.

8. K. D. Sheffler and G. S. Doble, "Influence of Creep Damage on the Low Cycle Thermal-Mechanical Fatigue Behavior of Two Tantalum Base Alloys," Final Report, Contract NAS 3-13228, NASA-CR-121001, TRW ER 7592, 1 May 1972.

APPENDIX A

SUPPLEMENTARY TESTS

All supplementary tests were conducted in ultrahigh vacuum using hourglass specimens identical to those used for fatigue tests. Tension tests were conducted at 1200°F (922°K) on 304 stainless steel, at 1100°F (866°K) on A-286, and at 600°F (589°K) on both alloys using a crosshead extension rate approximately half way between that associated with the high and low frequency isothermal fatigue tests. Properties measured were ultimate tensile strength and reduction of area. Creep tests were conducted at constant load on 304 stainless steel at 1200°F (922°K) and on A-286 at 1100°F (866°K). Reduction of area and rupture life were measured in these tests.

To evaluate the relative importance of creep and cold plastic flow in the elevated temperature fatigue tests, supplementary tests were conducted to determine the fraction of the reversed inelastic strain range which represented thermally activated deformation at the upper temperature level for each of the two test materials. These tests involved measurement of the inelastic strain range resulting from load limited strain controlled cycles at two different frequencies. The procedure involved repeated low frequency (0.0065 Hz) cycling at a specified diametral strain amplitude to develop a stabilized hysteresis loop, followed by high frequency cycling at a load range equivalent to that observed for the low frequency cycle. Based on the assumption that the inelastic strain developed in high frequency cycling was essentially all plastic*, the percentage of thermally activated deformation associated with the low frequency cycle was interpreted as the difference between the inelastic strain ranges at the two frequencies.

Results of the vacuum tensile and stress rupture tests are presented in Tables A-1 and A-2. Results of supplementary fatigue tests on 304 stainless steel are presented in Table A-3. The partitioning of the 304 stainless steel inelastic strain range into creep and plastic components at 1200°F (922°K) varied with total diametral strain range. Because there was no consistent pattern to these results, the ε_{cc} component for this material has been specified as the average of the three results presented in Table A-3, independent of total strain range. Efforts to partition the A-286 inelastic strain range at 1100°F (866°K) were unsuccessful. At equivalent load ranges, the total inelastic strain was larger at the high frequency than at the low frequency. No explanation could be developed for this apparent negative rate sensitivity.

- - - - - - - - - - - -

* This assumption was justified by comparsion of strain rates observed in the high frequency tests with equilibrium minimum creep rates for the two alloys at the largest stresses developed in the cyclic tests. For both alloys this difference was at least four orders of magnitude.

Table A-1

Tension Test Results

Test Material	Test Temperature °F	Test Temperature °K	Ultimate Tensile Strength ksi	Ultimate Tensile Strength MN/m^2	Percent Reduction of Area
304 SS	600	589	52.6	362	71
304 SS	1200	922	40.2	277	60
A-286	600	589	157.2	1083	29
A-286	1100	866	141.3	974	31

Table A-2

Creep Test Results

Material	Temperature °F	Temperature °K	Stress ksi	Stress MN/m^2	Rupture Life Hours	Percent Reduction of Area
304 SS	1200	922	18.7	129	835.7	60
A-286	1100	866	102.6	707	33.1	24

Table A-3

Strain-Range Partitioning Results on 304 SS Alloy

Total Low Frequency Diametral Strain Range	Percent ε_{cc}	Percent ε_{pp}
.0028	21	79
.0056	47	53
.0112	36	64
Average	35	65